Experimental determination of scattering matrices of dust particles at visible wavelengths: The IAA light scattering apparatus

O. Muñoz *, F. Moreno, D. Guirado, J.L. Ramos, A. López, F. Girela, J.M. Jerónimo, L.P. Costillo, I. Bustamante

Instituto de Astrofísica de Andalucía, CSIC, c/ Camino Bajo de Huétor 50, 18008 Granada, Spain

ARTICLE INFO

ABSTRACT

We present a new apparatus for measuring the complete scattering matrix as a function of the scattering angle of dust irregular particles. The design is based on the well-known apparatus located in Amsterdam, The Netherlands. In this improved version we have extended the scattering angle ranging from 3° to 177°. Moreover, the measurements are performed with a tunable argon–krypton laser that emit at a wavelength (λ) of 483, 488, 520, 568, or 647 nm. The apparatus has been developed at the Instituto de Astrofísica de Andalucía (IAA), Granada, Spain. To measure the scattering matrix elements we use a number of different optical components such as polarizers, a quarter-wave plate, and an electro-optic modulator. These components are used to manipulate the polarization state of light. By using eight different combinations for the orientation angles of the optical components, all scattering matrix elements are obtained as functions of the scattering angle. The accuracy of the instrument is tested by comparing the measured scattering matrices of water droplets at 488, 520, and 647 nm with Lorenz–Mie calculations for a distribution of homogeneous water droplets.

© 2009 Elsevier Ltd. All rights reserved.

1. Introduction

Irregular dust particles play an important role in the study of the Solar System, especially as far as planetary atmospheres and minor bodies are concerned [1]. Most solid particles in terrestrial and planetary atmospheres, and other solar system bodies such as asteroids and comets, consist of irregular mineral particles. These mineral particles seem to occur in a broad range of shapes and to be distributed in size from the sub-micron region up to millimeters (e.g. [2–6]). Light scattering is an important tool to retrieve information about the structure and origin of these celestial bodies and their atmospheres. Therefore, it is extremely important to study the light scattered by samples of polydisperse irregular particles.

Even with ever-increasing computer power and sophistication of algorithms, the characterization of cosmic dust from the observed scattered light remains an extremely difficult task due to the mentioned complicated morphology of these particles. Remarkable progress in developing advanced numerical algorithms for computing electromagnetic scattering by nonspherical particles has been achieved during the last decades (e.g. [7–17] and references therein). Still, many of these methods are restricted to quite simple particle geometries and specific size ranges. Consequently, controlled experimental studies of light scattering by irregular dust particles, remain a unique and indispensable tool for interpreting space- and ground-based observations.

There are several ways of studying the light scattered by mineral dust particles. One approach is to measure at visible wavelengths the phase function and degree of linear polarization for incident unpolarized light [18–22], or the full scattering matrix as a function of the scattering

* Corresponding author. Tel.: +34 958 121311; fax: +34 958 814530.
E-mail address: olga@iaa.es (O. Muñoz).

angle [23–26] of an ensemble of randomly oriented dust particles. In the last decades, the experimental setup located in Amsterdam, The Netherlands [27], has produced a significant amount of experimental data that are freely available in a digital form in the Amsterdam Light Scattering Database at http://www.astro.uva.nl/scatter [28,29]. It was capable of measuring all elements of the scattering matrix in the scattering angle ranging from about 3° to 174° at two different wavelengths (442 and 633 nm). Unfortunately, this setup was officially closed last year. In this paper we present an improved descendant of the Dutch experimental setup recently constructed at the Instituto de Astrofísica de Andalucía (IAA) in Granada, Spain. The Dutch instrument was designed in the 1980s. Therefore, the main improvements of the IAA apparatus derive from technical developments in the last decades. In the new apparatus the detectors have been designed so that the blockage of the laser beam at positions close to the forward and backward directions is minimum. This allows us to extend the measured scattering angle range from $\sim 3°-174°$ to $3°-177°$. Moreover, the accuracy of the measurements at small and large scattering angles has been improved by including in the measuring/reduction process corrections for the background signal. Additionally, we have extended the number of wavelengths of the incident light. In the IAA apparatus, we use a tunable argon–krypton laser (483, 488, 520, 568, and 647 nm) as a light source.

A review of the theory involved in these experiments is presented in Section 2. In Section 3, we give a detailed description of the new apparatus, including the data acquisition and reduction processes. The calibration measurements with water droplets are presented in Section 4. Future plans are discussed in Section 5.

2. The scattering matrix

The flux and state of linear and circular polarization of a quasi-monochromatic beam of light can be described by means of the so-called flux vector. If such a beam of light is scattered by an ensemble of randomly oriented particles separated by distances much larger than their linear dimensions and in the absence of multiple scattering, the flux vectors of the incident beam $\pi\boldsymbol{\Phi}_0(\lambda,\theta)$ and scattered beam $\pi\boldsymbol{\Phi}_{\text{det}}(\lambda,\theta)$, are for each scattering direction, related by a 4×4 matrix as follows [30,31]:

$$\boldsymbol{\Phi}_{\text{det}}(\lambda,\theta) = \frac{\lambda^2}{4\pi^2 D^2} \begin{pmatrix} F_{11} & F_{12} & F_{13} & F_{14} \\ F_{12} & F_{22} & F_{23} & F_{24} \\ -F_{13} & -F_{23} & F_{33} & F_{34} \\ F_{14} & F_{24} & -F_{34} & F_{44} \end{pmatrix} \boldsymbol{\Phi}_0(\lambda,\theta),$$

(1)

where the first elements of the column vectors are fluxes divided by π and the other elements describe the state of polarization of the beams by means of the Stokes parameters. Furthermore, θ, is the scattering angle, i.e., the angle between the directions of propagation of the incident and the scattered beams, λ is the wavelength, and D is the distance between the ensemble of particles and the detector. The scattering plane, i.e., the plane containing the directions of the incident and scattered beams, is the plane of reference for the flux vectors. The matrix **F**, with elements $F_{i,j}$, is called the scattering matrix of the ensemble of particles. The scattering matrix elements F_{ij} are dimensionless, and depend on the number and physical properties of the particles (size, shape, and refractive index), the wavelength of the incident light, and the scattering angle. For randomly oriented particles, all scattering planes are equivalent. Thus, the scattering direction is fully described by the scattering angle θ.

According to Eq. (1), a scattering matrix of randomly oriented particles has in general 10 different matrix elements. If, in addition, the ensemble presents equal amounts of particles and their mirror particles, the four elements $F_{13}(\theta)$, $F_{14}(\theta)$, $F_{23}(\theta)$, and $F_{24}(\theta)$ are zero over the entire scattering angle range (see e.g. [30]). The ensemble of particles in our experiment satisfy this condition. This leaves us with only six non-zero scattering matrix elements to be determined. For unpolarized incident light, $F_{11}(\theta)$ is proportional to the flux of the scattered light and is also called the phase function or the scattering function. Also, for unpolarized incident light, the ratio $-F_{12}(\theta)/F_{11}(\theta)$ equals the degree of linear polarization of the scattered light.

3. Experimental procedure

3.1. Experimental apparatus

In Fig. 1 we present a photograph of the IAA light scattering apparatus. The principle of the setup is similar to that developed by Hunt and Huffman [32]. The design of this new instrument is based on the Dutch instrument developed in the group of Hovenier in Amsterdam by Stammes [33], and Kuik [34], and subsequently revised and significantly improved by Volten et al. [35,36]. A detailed description of the Dutch instrument is given by Hovenier [27]. In this section we extensively describe the instrument including the main improvements with respect to the Dutch instrument.

An schematic overview of the experimental apparatus is presented in Fig. 2. Light from a linearly polarized continuous-wave tunable argon–krypton laser (that emit at λ equal to 483, 488, 520, 568, or 647 nm) passes through a polarizer (P) oriented at an angle γ_P and an electro-optic modulator (M) oriented at an angle γ_M (angles of optical elements are angles between their optical axes and the horizontal plane, measured counter-clockwise when looking in the direction of propagation of the light). The modulated light is subsequently scattered by randomly oriented particles located in a jet stream produced by either a nebulizer that produces water droplets, or an aerosol generator. Thus, no vessel is needed to contain the sample at the point where the scattering takes place. This is a great advantage, since anything between the particles and the detector decreases the accuracy of the measurements and limits the angular range. A filter wheel (FW) equipped with gray filters of different density is located between the laser and polarizer. It is operated from the computer so that the flux
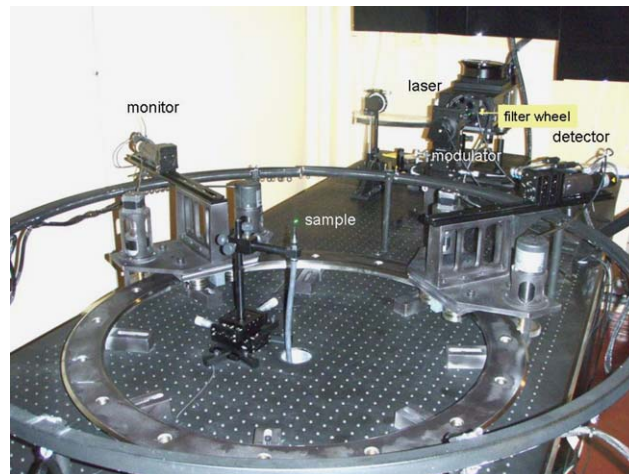
Fig. 1. Photograph of the experimental apparatus. On the right we can see the detector that moves along the ring. The ring is placed horizontally in the laboratory with an outer diameter of 1 m. The monitor is located on the left. In the middle, we see the nozzle of the nebulizer located vertically in the center of the ring, and the green spot is where the laser beam interacts with the aerosol cloud.
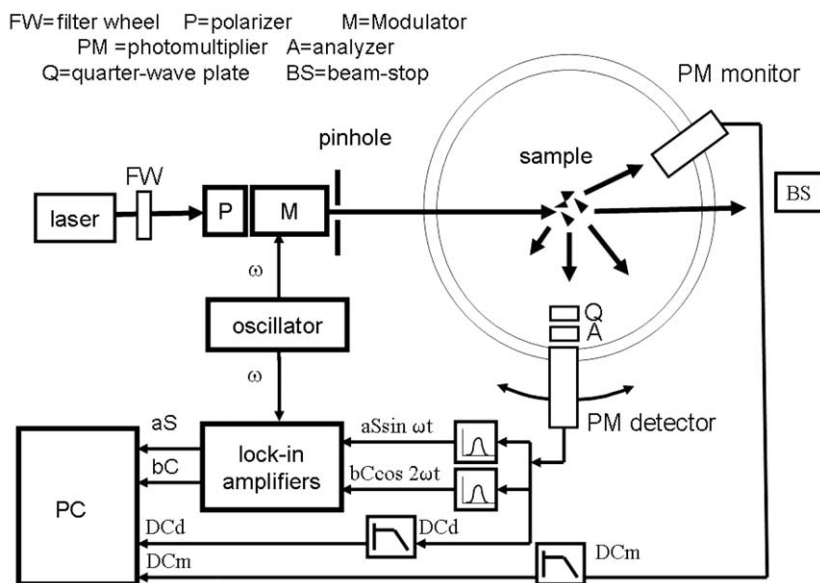

Fig. 2. Schematic overview of the experimental light scattering apparatus as seen from above. The detected signal is separated into its cDC and $aS \sin \omega t$ and $bC \cos 2\omega t$ components where $a = c1.383$ and $b = c0.8635$.

of the incident beam can be scaled to its most appropriate value for each scattering angle. The unscattered part of the incident beam is absorbed by a beam-stop.

The scattered light passes through a quarter-wave plate (Q) oriented at an angle γ_Q and an analyzer (A) oriented at an angle γ_A (both optional) and is detected by a photomultiplier tube (9828A Electron tubes©), the detector. The analyzer and quarter-wave plate are assembled to the photomultiplier by motorized rotating holders (DMT 40 OWIS©) controlled from the computer. In this way, we can orientate the optical axis of A, and Q with an accuracy of ∽8 arcsec. Another photomultiplier tube (the monitor)

is located at a fixed position and is used to correct for fluctuations in the aerosol stream. Detector and monitor are positioned on a ring with an outer diameter of 1 m with an angular resolution of 1/8°. This precision is obtained by using absolute rotary encoders of 12 bits. The detector moves along the ring in steps of 5°, or steps of 1° or even smaller if a higher angular resolution is required, covering a scattering angle range from 3° (nearly forward scattering) to 177° (nearly backward scattering). As shown in Fig. 1, the monitor and detector are mounted on dove tails so that they can be moved forward and backward. In this way, we can optimize the distance

between the detector and the sample. In case the flux of the scattered light is high enough, the detectors can be located further from the sample allowing us to measure at very small and very large scattering angles. In contrast, if the sample under study is not an efficient scatterer, i.e., the flux of the scattered light is very low, the detectors will be fixed closer to the sample improving the signal-to-noise ratio although decreasing the measurable scattering angle range. To carry out the experiments without ambient dust contamination, we have installed an inlet ceiling Luwa CG©. The ceiling produces a clean laminar airflow, creating a constant over-pressure in the experiment area and preventing an exchange with dirty outside air that could distort the measurement.

The electro-optic modulator in combination with lock-in detection, increases the accuracy of the measurements and allows simultaneous determination of several elements of the scattering matrix from the detected signal. The electro-optic modulator consists of a birefringent crystal in which a certain birefringence can be induced by applying an electric field. This causes the parallel and perpendicular components of a polarized beam of light to emerge from the modulator with an induced phase difference. If the voltage over the crystal is varied sinusoidally in time, the induced phase shift, ϕ, varies in the same way, i.e.,

$$\phi = \phi_m \sin \omega t, \tag{2}$$

where ϕ_m is the maximum phase shift and ω is the angular frequency of the voltage.

The Mueller matrix of a modulator with an orientation angle γ_M between the scattering plane and its principal axis is [37]

$$\mathbf{M}_{\gamma_M}(\phi) = \begin{bmatrix} 1 & 0 & 0 & 0 \\ 0 & C^2 + S^2 \cos \phi & SC(1 - \cos \phi) & -S \sin \phi \\ 0 & SC(1 - \cos \phi) & S^2 + C^2 \cos \phi & C \sin \phi \\ 0 & S \sin \phi & -C \sin \phi & \cos \phi \end{bmatrix}, \tag{3}$$

where $C = \cos 2\gamma_M$ and $S = \sin 2\gamma_M$. Since ϕ is itself a sinusoid, both $\sin \phi$ and $\cos \phi$ posses a complicated harmonic content which depends on the relative phase amplitude ϕ_m. The strength of each harmonic can be conveniently expressed as Fourier series of Bessel

functions (J_n) as follows:

$$\sin \phi = \sin(\phi_m \sin \omega t) = 2 \sum_{k=1}^{\infty} J_{2k-1}(\phi_m) \sin(2k - 1)\omega t, \tag{4}$$

$$\cos \phi = \cos(\phi_m \sin \omega t) = J_0(\phi_m) + 2 \sum_{l=1}^{\infty} J_{2l}(\phi_m) \cos 2l\omega t, \tag{5}$$

where only terms of frequency 2ω and lower are of further interest.

The flux vector reaching the detector, $\pi\boldsymbol{\Phi}_{\text{det}}(\lambda, \theta)$, is obtained by multiplying the flux vector of the incident light $\pi\boldsymbol{\Phi}_0(\lambda, \theta)$ by all Mueller matrices of the components in the optical train. Thus we have

$$\boldsymbol{\Phi}_{\text{det}}(\lambda, \theta) = c_1 \mathbf{A}_{\gamma_A} \mathbf{Q}_{\gamma_Q} \mathbf{F}(\theta) \mathbf{M}_{\gamma_M} \mathbf{P}_{\gamma_P} \boldsymbol{\Phi}_0(\lambda, \theta), \tag{6}$$

where c_1 is a real constant, and $\mathbf{A}$, $\mathbf{Q}$, $\mathbf{M}$, and $\mathbf{P}$, are the Mueller matrices of the analyzer, quarter wave plate, modulator and polarizer, respectively. $\mathbf{F}(\theta)$ is the scattering matrix of the ensemble of particles, and γ_A, γ_Q, γ_M, and γ_P are the orientation angles of the corresponding components. The amplitude of the sinusoidal signal applied to the modulator is adjusted so that the amplitude of the induced phase shift, ϕ_m, is the first zero of J_0, i.e., $\phi_m = 2.40483$ rad. The flux reaching the detector is then given by

$$\boldsymbol{\Phi}_{\text{det}}(\lambda, \theta) = c[DC(\theta) + 2J_1(\phi_m)S(\theta) \sin \omega t + 2J_2(\phi_m)C(\theta) \cos 2\omega t + \cdots], \tag{7}$$

where the coefficients $DC(\theta)$, $C(\theta)$, and $S(\theta)$ contain elements of the scattering matrix, $2J_1(\phi_m) = 1.0383$, $2J_2(\phi_m) = 0.8635$, and c is a constant that depends on the measuring conditions. By using lock-in amplifiers that are tuned to the first and second harmonic of ω the $2J_1(\phi_m)S(\theta) \sin \omega t$ and $2J_2(\phi_m)C(\theta) \cos 2\omega t$ terms can be selected. In our apparatus these two components together with the DC part of the detected signal are sufficient to determine all elements of the scattering matrix as functions of the scattering angle. The detected signal is then separated into $cDC(\theta)$ and each of the varying parts $c2J_1(\phi_m)S(\theta)$ and $c2J_2(\phi_m)C(\theta)$. The modulator voltage and the lock-in amplifiers are synchronized by using the same oscillator. Subsequently, we divide $c2J_1(\phi_m)S(\theta)$ and $c2J_2(\phi_m)C(\theta)$ by $cDC(\theta)$, belonging to the same configuration, so that the constant c is eliminated.

Table 1
Configurations of the orientation of polarizer P, modulator M, quarter-wave plate Q, and analyzer A used during the measurements.

Configuration	γ_P (deg)	γ_M (deg)	γ_Q (deg)	γ_A (deg)	$DC(\theta)$	$S(\theta)$	$C(\theta)$
1	90	−45	–	–	F_{11}	F_{14}	$-F_{12}$
2	90	−45	–	0	$F_{11} + F_{21}$	$F_{14} + F_{24}$	$-F_{12} - F_{22}$
3	90	−45	–	45	$F_{11} + F_{31}$	$F_{14} + F_{34}$	$-F_{12} - F_{32}$
4	90	−45	0	45	$F_{11} + F_{41}$	$F_{14} + F_{44}$	$-F_{12} - F_{42}$
5	45	0	–	–	F_{11}	$-F_{14}$	F_{13}
6	45	0	–	0	$F_{11} + F_{21}$	$-F_{14} - F_{24}$	$F_{13} + F_{23}$
7	45	0	–	45	$F_{11} + F_{31}$	$-F_{14} - F_{34}$	$F_{13} + F_{33}$
8	45	0	0	45	$F_{11} + F_{41}$	$-F_{14} - F_{44}$	$F_{13} + F_{43}$

The coefficients $DC(\theta)$, $S(\theta)$, and $C(\theta)$ correspond to DC, $\sin \omega t$, and $\cos 2\omega t$ components of the detector signal, respectively.

By using different combinations for the orientation angles of the optical components we are able to determine all relevant scattering matrix elements (see Table 1). Due to the lack of measurements between 0° and 3° and between 177° and 180°, we cannot measure the absolute angular dependency of the phase function, e.g. normalized to unity when averaged over all scattering directions. Instead, we normalize the measured phase function to unity at an arbitrary scattering angle (30°). We present the other scattering matrix elements divided by the original measured phase function.

3.2. Data acquisition

The measurement and reduction programs have been implemented in Labview 7.1, a programming language specific for instrumentation control. The program has been designed so that the pre-reduced data, i.e., the coefficient $DC(\theta)$ together with $S(\theta)$, and $C(\theta)$, divided by their corresponding $DC(\theta)$ value normalized to the signal of the monitor, are shown in the front panel of the program during the measurement run. In this way we are able to detect a possible error in, e.g. the alignment of the optics during a measurement run. This gives us the chance to interrupt the measurement run before completion thus avoiding the sample to be wasted in a spoiled measurement.

For each data point at a given scattering angle, 800 measurements are conducted in about 1 s. Therefore, one single data point is an average of 800 distinct measurements. The error of one data point is the standard deviation of the series of 800 measurements. To obtain good statistics we generally perform at least three measurement runs for each optical configuration. The obtained scattering matrix elements or combinations of matrix elements are the mean value of several data points and the adopted experimental error is the mean quadratic error of the selected data points. In some cases, due to the limited amount of sample material, there is just one data point per angle. In that case, the adopted error is due to the variation of the signal during the single series of 800 measurements. When a matrix element is not measured directly but is obtained from a measured combination of matrix elements (see Table 1 and [27]), its standard deviation is calculated by quadratic propagation of the directly measured matrix elements or combinations of matrix elements. The resulting experimental errors are indicated by error bars (see e.g. Figs. 4–7). We must note that accumulation of systematic errors due to small inaccuracies in the alignment of the optical elements, are not accounted for in the error bars.

3.3. Data reduction

First of all, obtaining the pre-reduced data mentioned in the previous section includes a correction for the inherent noise produced by the electronics involved in the data acquisition. As the noise may vary with time, a set of measurements in dark conditions at all possible amplification values is performed right before each measurement run. Thus, the values of the coefficients $DC(\theta)$, $S(\theta)$, and $C(\theta)$ are always corrected for the electronic noise of the amplification at which the data point has been obtained.

A traditional limitation of nephelometers is the lack of data at very small and very large scattering angles. There are two main technical reasons for such a limitation. On the one hand, at positions close to the forward direction, the laser light may be reflected by the holder of the detector distorting the actual measurements. On the other hand, when approaching the backward direction the detector blocks the laser beam. Moreover, the unscattered light of the incident beam that is reflected back by the beam-stop, strongly distorts the measurements at backward direction. To decrease the technical problems the detectors have been designed narrow enough to minimize the blockage of the laser beam at positions close to the forward and backward directions. Even so, the stray-light at forward and backward directions is significant. In addition, at short wavelengths Rayleigh scattering by gas molecules within the path beam also plays a role mainly at positions close to the forward and backward directions. To subtract the background signal from the measurements, we measure the contribution of background by doing an additional measurement with the aerosol jet turned off immediately after each actual measurement. In this way, we assure that the measuring conditions will be the same during both the measurements with aerosols and their corresponding background measurements. The coefficients corresponding to the background measurements, $DC_{backg}(\theta)$, $S_{backg}(\theta)$, and $C_{backg}(\theta)$ are subtracted from the coefficients of the aerosol measurements $DC(\theta)$, $S(\theta)$, and $C(\theta)$. An example of the resulting data before and after correcting the background corresponding to configuration 7 of Table 1, is presented in Fig. 3. As shown, the background signal is significant at 3° and close to the backward direction.

From the pre-reduced data corrected for inherent noise and background, the $F_{11}(\theta)$ is normalized to 1 at 30° and the scattering matrix element ratios $F_{ij}(\theta)/F_{11}(\theta)$ with i, $j = 1$–4 ($i = j \neq 1$) are extracted from the measured $DC(\theta)$, $S(\theta)$, and $C(\theta)$ coefficients by following the description given by Hovenier [27].

Once we have the reduced experimental 4×4 scattering matrix, $\mathbf{F}(\theta)$, we check that the measured matrix can be a sum of pure scattering matrices. The reduction program verifies the reliability of the measurements by applying the Cloude coherency matrix test as suggested by Hovenier and van der Mee [38].

4. Calibration measurements

The reliability of the measurements is tested by comparing results of water droplets measurements to results of Lorenz–Mie calculations for a distribution of homogeneous spherical particles. As a starting point we have constrained the calibration measurements to the wavelengths of 488, 520, and 647 nm since the other wavelengths are too close to each other to develop any significant differences in the Lorenz–Mie calculations. However, in case a special sample/project would require
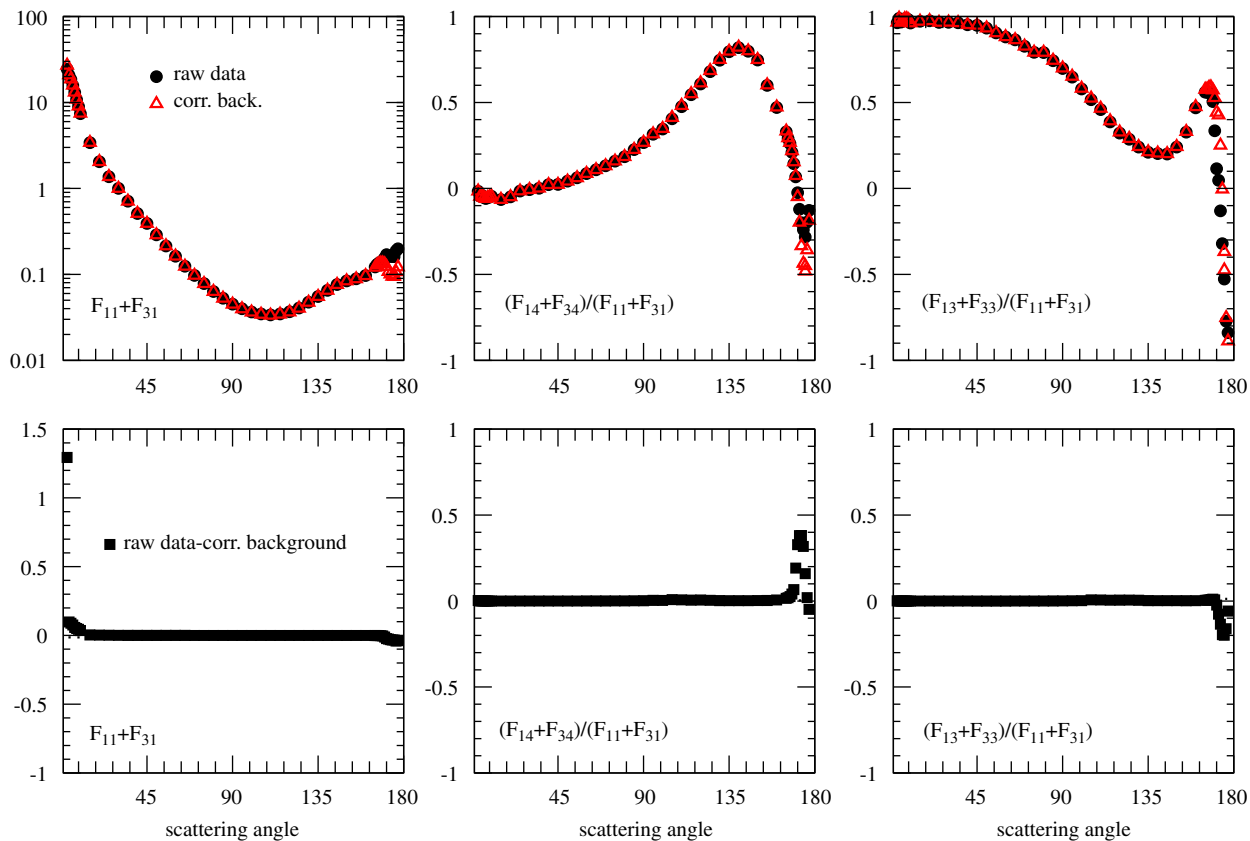
Fig. 3. Upper panels: intermediate results of the data reduction process for the optical configuration 7 in Table 1. Full circles denote the pre-reduced raw (uncorrected) data. The corresponding pre-reduced data corrected for background (corr.back.) are denoted by open triangles. Lower panels: full squares correspond to the measured differences of the *DC*, $S(\theta)$, and $C(\theta)$ of the corrected and uncorrected data, respectively.

it, we are able to perform the measurements at the other emission wavelengths of the argon–krypton laser, i.e., 483 and 568 nm.

As mentioned in Section 3.1, the water droplets are produced by a nebulizer. For the Lorenz–Mie calculations, we assume a log-normal size distribution. In the fitting procedure, the refractive index of water is assumed as a fixed parameter at the three studied wavelengths ($m = 1.33 - 0.0i$). The two parameters that define the size distribution, σ_g and r_g are defined as [39]

$$\ln r_g = \int_0^\infty \ln r n(r) \, dr, \tag{8}$$

$$\sigma_g^2 = \int_0^\infty (\ln r - \ln r_g)^2 n(r) \, dr, \tag{9}$$

where $n(r) \, dr$ is the fraction of the total number of equivalent spheres with radii between r and $r + dr$ per unit volume of space. They are chosen so that the differences between the measured and the calculated values for the $F_{11}(\theta)$ and $-F_{12}(\theta)/F_{11}(\theta)$ are minimized. The method to find the best-fitted values for r_g and σ_g is based on the downhill simplex method of Nelder and Mead [40], particularly the FORTRAN implementation described in the Numerical Recipes book [41], subroutine

AMOEBA. The method is independently applied to fit the $F_{11}(\theta)$ and $-F_{12}(\theta)/F_{11}(\theta)$ at the three studied wavelengths, namely 488, 520, and 647 nm. The averaged values obtained from the best fits for the six studied functions give a value of $\sigma_g = 1.50 \pm 0.04$ and $r_g = 0.80 \pm 0.07 \, \mu m$.

In Figs. 4–6, we present the measured and the calculated scattering matrices as functions of the scattering angle at λ equal to 488, 520, and 647 nm, respectively. The measured and the calculated $F_{11}(\theta)$ are plotted on a logarithmic scale and normalized to 1 at 30°. The other matrix elements are plotted relative to $F_{11}(\theta)$. We refrain from showing the four element ratios $F_{13}(\theta)/F_{11}(\theta)$, $F_{14}(\theta)/F_{11}(\theta)$, $F_{23}(\theta)/F_{11}(\theta)$, and $F_{24}(\theta)/F_{11}(\theta)$, since we verified that these ratios do not differ from zero by more than the error bars, in accordance with Lorenz–Mie theory. The measurements satisfy the Cloude coherency matrix test at all measured scattering angles.

As shown in Figs. 4–6, the water droplet measurements show an excellent agreement with the Lorenz–Mie computations over the entire angle range at the three studied wavelengths. The small deviations may at least partly be due to differences in the size distributions and
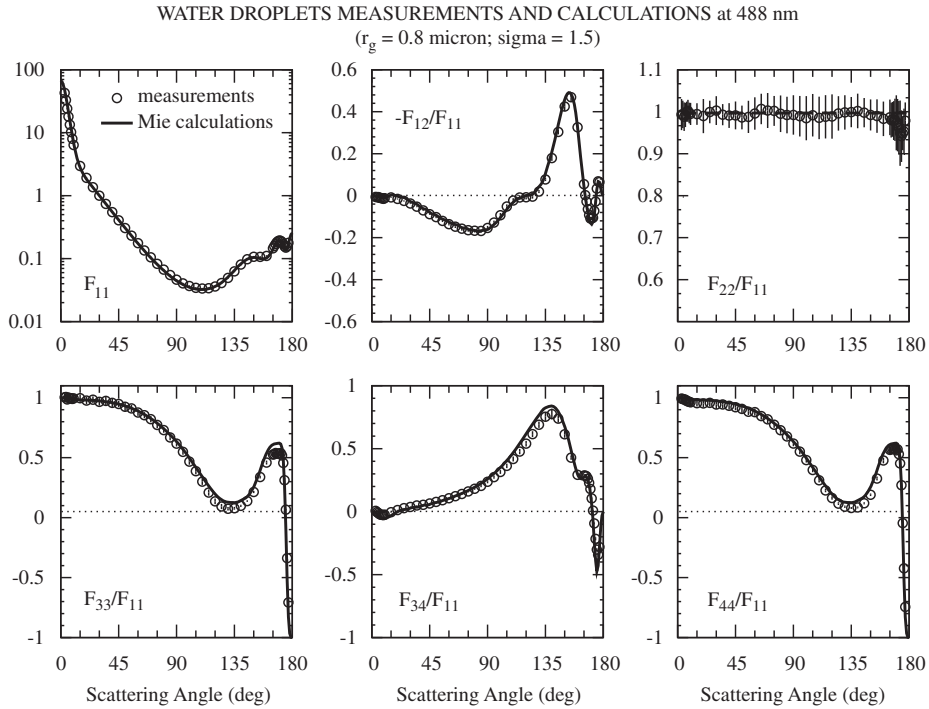
WATER DROPLETS MEASUREMENTS AND CALCULATIONS at 488 nm
(r$_g$ = 0.8 micron; sigma = 1.5)

Fig. 4. Scattering matrix elements $F_{11}(\theta)$, normalized to 1 at 30°, element ratios $-F_{12}(\theta)/F_{11}(\theta)$, $F_{22}(\theta)/F_{11}(\theta)$, $F_{33}(\theta)/F_{11}(\theta)$, $F_{34}(\theta)/F_{11}(\theta)$, and $F_{44}(\theta)/F_{11}(\theta)$ for water droplets at $\lambda = 488$ nm. Solid lines correspond to results of Lorenz–Mie calculations at 488 nm for a log-normal size distribution ($r_g = 0.8\,\mu$m and $\sigma_g = 1.5$). Errors are presented by bars that sometimes are not seen because they are within the size of the symbols.

WATER DROPLETS MEASUREMENTS AND CALCULATIONS at 520 nm
(r$_g$ = 0.8 micron; sigma = 1.5)
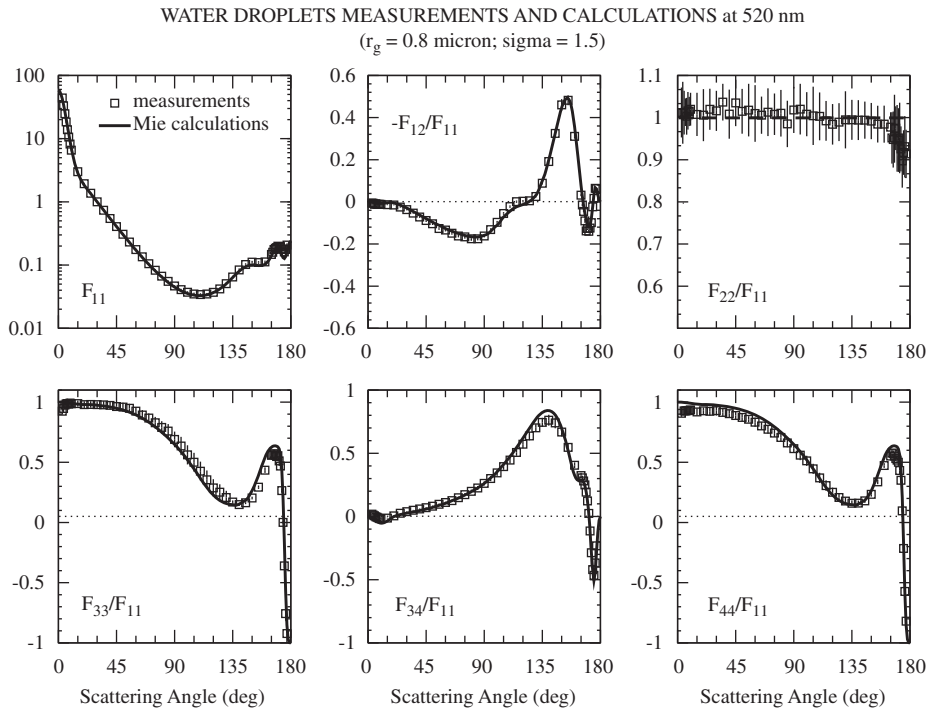
Fig. 5. Same as Fig. 4 but at $\lambda = 520$ nm.

WATER DROPLETS MEASUREMENTS AND CALCULATIONS at 647 nm
($r_g = 0.8$ micron; sigma = 1.5)
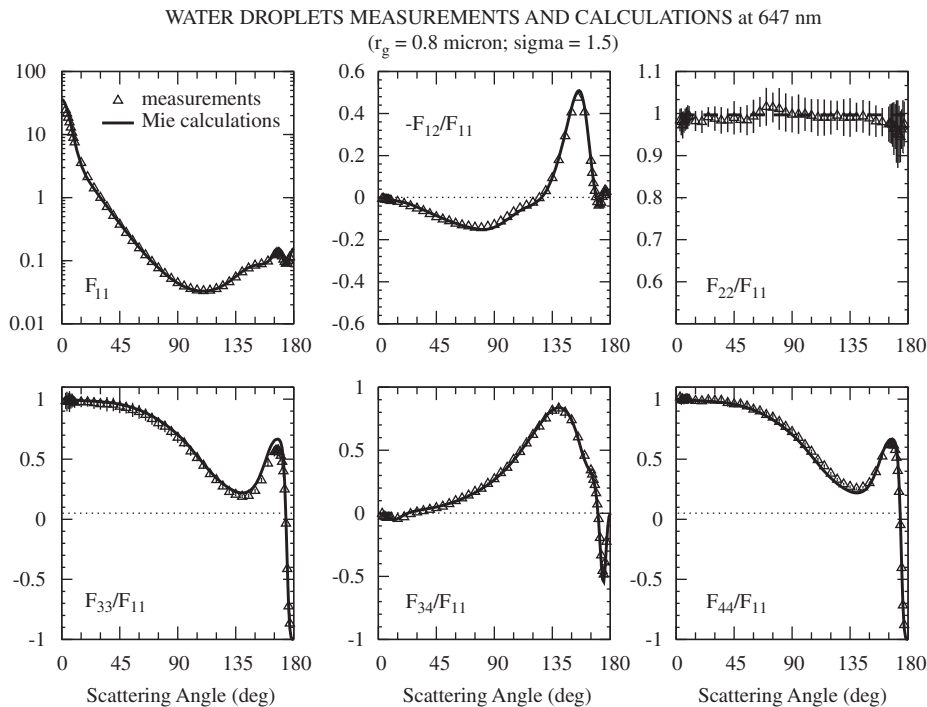
Fig. 6. Same as Fig. 4 but at $\lambda = 647$ nm.

the not perfectly spherical shape of the water droplets used in the experiments. The experimental data exhibit the typical behavior of a distribution of homogeneous spherical particles, i.e., $F_{22}(\theta)/F_{11}(\theta)$ is equal to unity at all scattering angles. In addition, the $F_{33}(\theta)/F_{11}(\theta)$ and $F_{44}(\theta)/F_{11}(\theta)$ ratios are identical to one another at all scattering angles.

In Fig. 7, we present enlargements of the minor features seen in the measured phase function $F_{11}(\theta)$, degree of linear polarization for incident unpolarized light $-F_{12}(\theta)/F_{11}(\theta)$, and the $F_{33}(\theta)/F_{11}(\theta)$, and $F_{44}(\theta)/F_{11}(\theta)$ ratios at the two extreme wavelengths, 488 and 647 nm. The measurements are presented together with the Lorenz–Mie calculations. As seen in Fig. 7, even the minor features presented in the measurements are very well reproduced by the Lorenz–Mie calculations. For instance, the measured phase functions develop a small peak at 170° and 168° in the blue and red light, respectively. Moreover, a soft increase in the phase function is presented at positions close to the backward direction reaching higher values in the blue than in the red. The measured degrees of linear polarization present a negative branch in the backscattering region. This negative branch is significantly deeper at 488 nm (∽11%) than at 647 nm (∽4%). Furthermore, the measured $-F_{12}(\theta)/F_{11}(\theta)$ presents a flat dependence on the scattering angle between 115° and 125° at 488 nm. This flat region is not shown in the measurements at 647 nm. Besides, the minimum of the $F_{33}(\theta)/F_{11}(\theta)$ ratio (and consequently the $F_{44}(\theta)/F_{11}(\theta)$) at side scattering angles is deeper at 488 nm than at 647 nm.

5. Summary and outlook

We present a new laboratory apparatus for measuring the complete scattering matrix as a function of the scattering angle of aerosol particles. This new instrument is an improved descendant of the experimental setup located in Amsterdam for many years [27]. We have extended the scattering angle range from ∼3°−174° to 3°−177°. Apart from the new design of the detectors, the accuracy of the measurements at small and large scattering angles has been improved by including in the measuring/reduction process corrections for the background signal. The number of wavelengths has been increased from two to five, namely 483, 488, 520, 568, and 647 nm. Moreover, the instrument and measuring program have been designed to perform faster and more efficient measurements allowing us to work with smaller amounts of sample. The accuracy of the system has been tested by comparison of the measured scattering matrices for water droplets at 488, 520, and 647 nm, with results of Lorenz–Mie calculations for homogeneous spherical water droplets. The apparatus is devoted to experimentally studying the angle-dependent scattering matrices of dust samples of astrophysical interest. We are specially interested in mineral dust particles that are potential candidates for being present in the planetary and cometary atmospheres of the Solar System (e.g. olivines, pyroxenes, calcite, carbon, etc.). Moreover, there is a great interest in measuring aerosol samples that can affect the radiative balance of the Earth's atmosphere such as desert dust, volcanic ashes, and carbon soot.
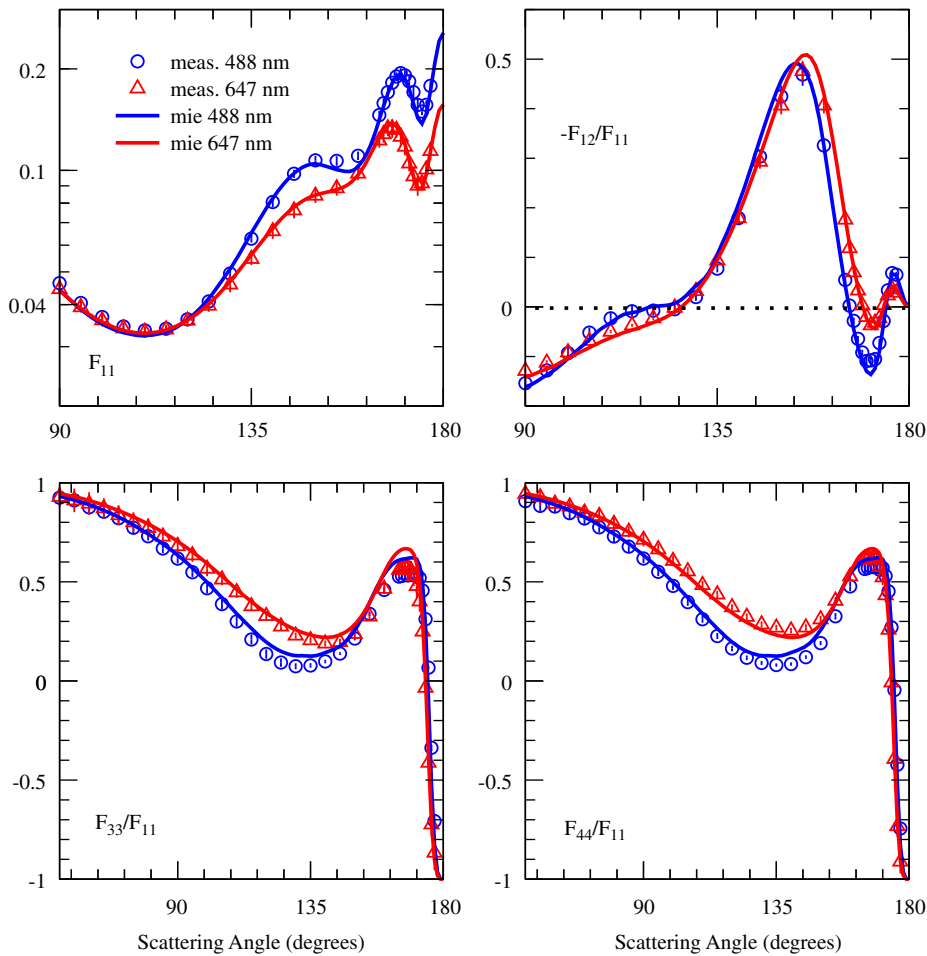
Fig. 7. Enlargements of the $F_{11}(\theta)$, $-F_{12}(\theta)/F_{11}(\theta)$, $F_{33}(\theta)/F_{11}(\theta)$, and $F_{44}(\theta)/F_{11}(\theta)$ at the wavelengths 488 and 647 nm, showing the outstanding agreement between the measured and the calculated values.

Acknowledgments

References

[1] Hovenier JW, Muñoz O. Light scattering in the Solar System: an introductory review. JQSRT 2009; 100(14–16):1280–92.

[2] d'Almeida GA, Koepke P, Shettle EP. Atmospherical aerosols: global climatology and radiative characteristics. Hampton, VA: A.Deepak; 1991.

[3] Muñoz O, Moreno F, Molina A, Ortiz JL. A comparison of the structure of the aerosol layers in the great red SPOT of Jupiter and its surroundings before and after the 1993 SEB disturbance. Astron Astrophys 1999;344:355–61.

[4] Fulle M. Motion of cometary dust. In: Festou MC, Keller HU, Weaver HA, editors. Comets II. University of Arizona Press; 2004. p. 565–75.

[5] Wolff MJ, Smith MD, Clancy RT, Spanovich N, Whitney BA, Lemmon MT, et al. Constraints on dust aerosols from the Mars exploration rovers using MGS overflights and Mini-TES. J Geophys Res 2006;111(E12) [CiteID E12S17].

[6] Nousiainen T. Optical modeling of mineral dust particles: a review. JQSRT 2009;110(14–16):1261–79.

[7] Mishchenko MI, Travis LD, Mackowski DW. T-matrix computations of light scattering by nonspherical particles: a review. JQSRT 1996;55:535–75.

[8] Muinonen K, Nousiainen T, Fast P, Lumme K. Ray optics regime for Gaussian random spheres. JQSRT 1997;57:197–205.

[9] Mishchenko MI, Hovenier JW, Travis LD. Light scattering by non spherical particles: theory, measurements, and applications. San Diego: Academic Press; 2000.

[10] Mishchenko MI, Travis LD, Lacis AA. Scattering, absorption, and emission of light by small particles. Cambridge: Cambridge University Press; 2002.

[11] Draine BT, Flatau PJ. User guide for the discrete dipole approximation code DDSCAT 6.0. ⟨http://arxiv.org/abs/astro-ph/0309069⟩; 2003.

[12] Kahnert FM. Numerical methods in electromagnetic scattering theory. JQSRT 2003;79:775–824.

[13] Taflove A, Hagness SV. Advances in computational electrodynamics: the finite-difference time-domain method. 3rd ed. Boston: Artech House; 2005.

[14] Yurkin MA, Hoekstra AG. The discrete dipole approximation: an overview and recent developments. JQSRT 2007;106:558–89.

[15] Mishchenko MI. Electromagnetic scattering by nonspherical particles: a tutorial review. JQSRT 2009;110(11):808–32.

[16] Muinonen K, Nousiainen T, Lindqvist A, Muñoz O, Videen G. Light scattering by Gaussian particles with internal inclusions and roughened surfaces using ray optics. JQSRT 2009;110(14–16):1628–39.

[17] Wriedt T. Light scattering theories and computer codes. JQSRT 2009;110(11):833–43.

[18] Jaggard DL, Hill C, Shorthill RW, Stuart RW, Glantz M, Rossworg F, et al. Light scattering from particles of regular and irregular shape. Atmos Environ 1981;15:2511–9.

[19] Weiss-Wrana K. Optical properties of interplanetary dust—comparison with light scattering by larger meteoritic and terrestrial grains. Astron Astrophys 1983;126:240–50.

[20] West RA, Doose LR, Eibl AM, Tomasko MG, Mishchenko MI. Laboratory measurements of mineral dust scattering phase function and linear polarization. J Geophys Res 1997;102(D14):16871–82.

[21] Curtis DB, Meland B, Aycibin M, Arnold N, Grassian VH, Young M, et al. A laboratory investigation of light scattering from representative components of mineral dust aerosol at a wavelength of 550 nm. J Geophys Res 2008;113(D8) [CiteID D08210].

[22] Hadamcik E, Renard JB, Levasseur-Regourd AC, Lasue J, Alcouffe G, Francis M. Light scattering by agglomerates: interconnecting size and absorption effects (PROGRA2). JQSRT 2009:110(14–16):1755–70.

[23] Holland AC, Gagne G. The scattering of polarized light by polydisperse systems of irregular particles. Appl Opt 1970;9(5):1113–21.

[24] Perry RJ, Hunt AJ, Huffman DR. Experimental determination of Mueller scattering matrices for nonspherical particles. Appl Opt 1978;17:2700–10.

[25] Muñoz O, Volten H, Hovenier JW, Nousiainen T, Muinonen K, Guirado D, et al. Scattering matrix of large Saharan dust particles: experiments and computations. J Geophys Res 2007;112(D13) [CiteID D13215].

[26] Volten H, Muñoz O, Hovenier JW, Rietmeijer FJM, Nuth JA, Waters LBFM, et al. Experimental light scattering by fluffy aggregates of magnesiosilica, ferrosilica, and alumina cosmic dust analogs. Astron Astrophys 2007;470:377–86.

[27] Hovenier JW. Measuring scattering matrices of small particles at optical wavelengths. In: Mishchenko MI, Hovenier JW, Travis LD, editors. Light scattering by nonspherical particles. San Diego, CA: Academic Press; 2000. p. 355–65.

[28] Volten H, Muñoz O, Hovenier JW, de Haan JF, Vassen W, van der Zande WJ, et al. WWW scattering matrix database for small mineral particles at 441.6 and 632.8 nm. JQSRT 2005;90(2):191–206.

[29] Volten H, Muñoz O, Hovenier JW, Waters LBFM. An update of the Amsterdam light scattering database. JQSRT 2006;100:437–43.

[30] Van de Hulst HC. Light scattering by small particles. New York: Wiley; 1957.

[31] Hovenier JW, van der Mee CVM, Domke H. Transfer of polarized light in planetary atmospheres: basic concepts and practical methods. Dordrecht: Kluwer, Springer; 2004.

[32] Hunt AJ, Huffman DR. A new polarization-modulated light scattering instrument. Rev Sci Instrum 1973;44(12):1753–62.

[33] Stammes P. Light scattering properties of aerosols and the radiation inside a planetary atmosphere. PhD dissertation 1989, Free Univesity, Amsterdam.

[34] Kuik F. Single scattering by ensembles of particles with various shapes. PhD dissertation 1992, Free University, Amsterdam.

[35] Volten H. Light scattering by small particles. An experimental study. PhD dissertation 2001, Free University, Amsterdam.

[36] Volten H, Muñoz O, Rol E, de Haan JF, Vassen V, Hovenier JW, et al. Scattering matrices of mineral aerosol particles at 441.6 nm and 632.8 nm. J Geophys Res 2001;106:17375–401.

[37] Collett E. Polarized light—fundamentals and applications. Optical engineering series, vol. 36. New York: Marcel Dekker; 1993.

[38] Hovenier JW, van der Mee CVM. Testing scattering matrices, a compendium of recipes. JQSRT 1996;55:649–61.

[39] Hansen JE, Travis LD. Light scattering in planetary atmospheres. Space Sci Rev 1974;16:527–610.

[40] Nelder A, Mead R. A simplex method for function minimization. Comput J 1965;7:308–13.

[41] Press W, Teukolsky S, Vetterling W, Flannery B. Numerical recipes in Fortran 77, 2nd ed., 1992. ISBN 0-521-43064-X 1992.